Rock Mech Rock Eng (2011) 44:179–198
DOI 10.1007/s00603-010-0116-3

ORIGINAL PAPER

Numerical Study of Failure Mechanism of Serial and Parallel Rock Pillars

S. Y. Wang · S. W. Sloan · M. L. Huang · C. A. Tang

Received: 9 November 2009 / Accepted: 2 September 2010 / Published online: 16 September 2010

Abstract Using a numerical modelling code, rock failure process analysis, 2D, the progressive failure process and associated acoustic emission behaviour of serial and parallel rock samples were simulated. Both serial- and parallel sample models are presented for investigating the mechanism of rock pillar failure. As expected, the numerical results show that not only the stiffness, but also the uniaxial compressive strength of the rock plays an important role in pillar instability. For serial pillars, the elastic rebound of a rock pillar with higher uniaxial compressive strength can lead to the sudden failure of an adjacent rock pillar with lower uniaxial compressive strength. The failure zone forms and develops in the pillar with lower uniaxial compressive strength; however, the failure zone does not pass across the interface of the two pillars. In comparison, when two pillars have the same uniaxial compressive strengths but different elastic moduli, both serial pillars fail, and the failure zone in the two pillars can interact, passing across the interface and entering the other pillar. For parallel pillars, damage always develops in the pillar having the lower uniaxial compressive strength or lower elastic modulus. Furthermore, in accordance with the Kaiser effect, the stress-induced damage in a rock pillar is irreversible, and only when the previous stress state in the failed rock pillar is exceeded or the subsequent applied energy is larger than the energy released by the external loading will further damage continue to occur. In addition, the homogeneity index of rock also can affect the failure modes of parallel pillars, even though the uniaxial compressive strength and stiffness of each pillar are the same.

Keywords Serial and parallel · Numerical simulation · Damage · Acoustic emission

S. Y. Wang (✉) · S. W. Sloan
Centre for Geotechnical and Materials Modelling,
Civil, Surveying and Environmental Engineering,
The University of Newcastle, Callaghan, NSW 2308, Australia
e-mail: Shanyong.Wang@newcastle.edu.au

S. W. Sloan
e-mail: Scott.Sloan@newcastle.edu.au

M. L. Huang
School of Civil Engineering, Beijing Jiaotong University,
Beijing 100044, People's Republic of China
e-mail: huang1969@vip.sina.com

C. A. Tang
School of Civil and Hydraulic Engineering,
Dalian University of Technology, Dalian 116024,
People's Republic of China
e-mail: catang@mechsoft.cn

1 Introduction

Pillars are used in a mine to support the weight of overburden material between adjacent underground openings. As mine depths increase, pillar failure becomes more frequent and critical due to the progressive increase in ambient stresses (Cook 1976). This failure process is a progressive one due to the initiation and propagation of cracks, disturbance of local stress fields, development of local failures and the formation of fracture planes. These micro processes lead to macroscopic pillar failure and the associated loss of load-carrying capability (Fang and Harrison 2002).

In laboratory tests, the pillar-failure mechanism can be investigated by uniaxial compression loading in a stiff testing machine (Gill et al. 1993). Indeed, servo-controlled testing machines provide a valuable means of initiating the failure of rock specimens under a prescribed deformation rate. However, the occurrence of instability during rock

failure depends on the stiffness ratio of the rock to the machine (Hudson et al. 1972), which can complicate the interpretation of the results. In general, the occurrence of soft rocks in the roof or floor of a mine accelerates the failure process by quickly releasing the energy stored in the pillar system when a high-strength pillar penetrates into the failed material (Tang et al. 1993).

Under actual field conditions, the pillar load capacity is reduced to a residual value and failure occurs once the applied stress level exceeds its peak uniaxial compressive strength. From a design point of view, understanding the pillar-failure mechanism is essential. The pillar strength can be assessed using empirical, statistical or analytical methods (Sheorey 1993). For example, some authors have proposed empirical and semi-statistical approaches for calculations of the uniaxial compressive strength of pillar (Salamon 1970; van der Merwe 1998). However, due to the nonlinear behaviour of rock pillars at the high stress levels associated with deep mining conditions, the failure mechanism is not considered explicitly in these methods. Moreover, as evident from the Kaiser (1950) effect, the stress-induced damage in a rock pillar is irreversible. A further complication is that parallel pillars may fail at different times, leading to probable interaction effects between adjacent damaged pillars. The failure mechanisms can also be different for each individual pillar, owing to the heterogeneous character of the rock mass. As a result, it is not easy to predict the final uniaxial compressive strength of the pillars.

Compared with simplified laboratory tests and analytical methods, numerical methods have the advantage of being able to model complex boundary conditions and material properties, as well as the mechanisms involved in rock pillar failure (Mortazavi et al. 2009). Murali Mohan et al. (2001) used FLAC^{3D} to simulate failed and stable pillars in Indian coal mines. Chen et al. (2009) numerically investigated the effects of rock pillar width on the stability behaviour of three and four parallel tunnels during excavation. The numerical results showed that the interaction effects were dependent not only on the geological conditions and tunnel cross section, but also on the rock pillar widths. In addition, Chen et al. (1997) and Kaiser and Tang (1998) provided a double-rock sample model for studying the pillar rockburst mechanism and simulated the progressive failure process in a pillar. However, the different mechanical properties and the further interactions between pillars with different uniaxial compressive strengths and stiffnesses during the failure process were not considered.

Rock pillars in general have 3-D geometries. However, according to Mortazavi et al. (2009), for narrow-vein mining conditions, where the ore body is nearly vertical and very long, the pillar behaviour can be modelled under plane strain conditions. In the present investigation, the numerical modelling code rock failure process analysis (RFPA) is used to simulate the failure mechanism of rock pillars. The focus of the work is to study the failure processes of pillars in serial and parallel, as well as their corresponding stress–strain behaviour. In addition, the effect of rock heterogeneity on the failure mechanism is also considered.

2 Brief Description of RFPA and Model Setup

Briefly, RFPA2D (Tang 1997) is a two-dimensional finite element code that can simulate the fracture and failure process of quasi-brittle materials such as rock. To model the failure of a rock material (or a rock mass), the medium is assumed to be composed of many mesoscopic elements with differing material properties, which are specified according to a Weibull distribution. The finite element method is employed to obtain the stress fields in these mesoscopic elements. Linear elastic damage mechanics is used to describe the constitutive law of the meso-scale elements, and the maximum tensile-strain criterion and the Mohr–Coulomb criterion are utilized as damage thresholds (Zhu and Tang 2004).

As rock is a heterogeneous material; it is assumed that the local mechanical parameters are distributed following a certain probability distribution. Weibull's distribution describes the experimental data obtained for the distribution of heterogeneities in rock very well (Weibull 1939). Here, it is assumed that the specimen is divided into many finite elements and the elemental parameters (uniaxial compressive strength, σ_c, elastic modulus, E, etc.) of the rock follow Weibull's distribution law:

$$\varphi(\sigma) = \frac{m}{\sigma_{ca}}\left(\frac{\sigma_c}{\sigma_{ca}}\right)^{m-1}\exp\left[-\left(\frac{\sigma_c}{\sigma_{ca}}\right)^{m}\right] \quad (1)$$

$$\varphi(E) = \frac{m}{E_a}\left(\frac{E}{E_a}\right)^{m-1}\exp\left[-\left(\frac{E}{E_a}\right)^{m}\right] \quad (2)$$

where σ_{ca} and E_a are the average uniaxial compressive strength and elastic modulus, respectively, and m is the shape parameter. The shape parameter m is defined as the homogeneity index of the rock (Tang et al. 1993, 1997; Tang 1997), with a larger m implying a more homogeneous material and vice versa.

In the proposed model, a damage mechanics approach is employed to model the mechanical behaviour of the meso-scale elements. For each element, the material is assumed to be linear elastic, isotropic and undamaged before loading, with its elastic properties defined by the elastic modulus and Poisson's ratio. After the initiation of damage, the uniaxial compressive strength and elastic modulus of the element are assumed to degrade gradually with the elastic

modulus of the damaged material given by (Krajcinovic 1996):

$$E = (1 - D)E_0 \tag{3}$$

where E and E_0 are the elastic moduli of the damaged material and the undamaged material, respectively, and D is the damage variable, ranging from zero (for the undamaged material) to one (for the completely damaged state). The constitutive law for the damaged rock under uniaxial stress conditions can then be expressed as (Krajcinovic 1996; Tang et al. 1997)

$$\sigma = E\varepsilon(1 - D) \tag{4}$$

where ε is the strain. Two kinds of damage thresholds are adopted: the maximum tensile-strain criterion and the Mohr–Coulomb shear strength criterion (Zhu and Tang 2004; Tang 1997).

When the maximum tensile strain criterion is met, damage of the element occurs. Herein, this kind of damage is called tensile damage and D is given by Zhu and Tang (2004):

$$D = \begin{cases} 0 & \varepsilon < \varepsilon_{t0} \\ 1 - \frac{\sigma_{tr}}{E_0\varepsilon} & \varepsilon_{t0} \le \varepsilon < \varepsilon_{tu} \\ 1 & \varepsilon \ge \varepsilon_{tu} \end{cases} \tag{5}$$

where σ_{tr} is the residual tensile strength, ε is the tensile strain, ε_{t0} is the tensile strain at the elastic limit (the so-called threshold strain) and ε_{tu} is the ultimate tensile strain corresponding to the completely damaged state of the material (Zhu and Tang 2004).

In addition, the Mohr–Coulomb criterion is included as the second damage threshold to detect shear damage. This criterion is given by the following equation (Zhu and Tang 2004):

$$F = \frac{1 + \sin\phi}{1 - \sin\phi}\sigma_1 - \sigma_3 \ge \sigma_{c0} \tag{6}$$

where σ_1 and σ_3 are the major and minor principal stresses, respectively, σ_{c0} is the uniaxial compressive strength, and φ is the angle of internal friction (Zhu and Tang 2004). Amitrano (1999) used this kind of shear failure criterion to investigate the damage of rock with an isotropic damage threshold.

In this case, the damage variable D is given by (Zhu and Tang 2004):

$$D = \begin{cases} 0 & \varepsilon < \varepsilon_{c0} \\ 1 - \frac{\sigma_{cr}}{E_0\varepsilon} & \varepsilon \ge \varepsilon_{c0} \end{cases} \tag{7}$$

where σ_{cr} is the residual uniaxial compressive strength and ε_{c0} is the strain at the peak value of maximum principal stress.

It is assumed that $\sigma_{cr}/\sigma_{c0} = \sigma_{tr}/\sigma_{t0} = \lambda$ when an element is under uniaxial compression or tension, where σ_{t0} is the uniaxial tensile strength and λ is a residual strength coefficient, which lies in the range $0 < \lambda \le 0.1$. Detailed descriptions of these parameters can be found in Zhu and Tang (2004) and Wang et al. (2006, 2009).

There is a strong link between rock damage and acoustic emission (AE). AE indicates the extent of local damage in rocks, which is directly associated with the evolution and propagation of fracturing. Tang et al. (1997) derived the following relationship between the damage parameter D and the AE counts, N:

$$D = \frac{N}{N_m} \tag{8}$$

where N_m is the accumulated AE count. By recording the counts of failed elements (i.e. elements in which all the Gauss points have failed) and the released energy when failure occurs, the AE phenomena associated with progressive failure can be simulated.

Figure 1 shows a schematic of the numerical model for serial and parallel pillars. We examine three principal parameters in Eqs. 1 and 2: the uniaxial compressive strength (σ_c), the elastic modulus (E) and the homogeneity index (m). In total, three types of numerical models are studied. The first type, Type I is the serial model (Fig. 1a), which examines the effect of the uniaxial compressive strength and elastic modulus of each rock pillar on the failure mode, keeping the other parameters such as Poisson's ratio and the homogeneity index (m) constant. Case I is for pillars of different uniaxial compressive strengths but the same elastic modulus, and Case II considers those with the same uniaxial compressive strength but different elastic moduli. The input parameters are listed in Table 1. The second type, Type II, analyses the parallel model (Fig. 1b), again with Case I being for different uniaxial compressive strengths but the same elastic modulus, and Case II being for the same uniaxial compressive strength but different elastic moduli. The input parameters are listed in Table 2. Finally, for Type III (Fig. 1c), the effect of the homogeneity index (m) on the failure mode of pillars is examined by keeping the uniaxial compressive strength, the elastic modulus and Poisson's ratio constant. In this instance, Case I is for pillars 1, 2 and 3 with different homogeneity indices (m) of 4, 5 and 3, respectively. Case II considers each pillar with the same homogeneity index of 3. The input parameters are listed in Table 3. Since the effects of the stiffness/uniaxial compressive strength of the floor and roof on the pillar-failure mode has been studied by Kaiser and Tang (1998), the current investigation focuses on the interaction of pillars in serial and parallel with different uniaxial compressive strengths, elastic moduli and homogeneity indices (m). For simplicity, the uniaxial tensile strength is assumed to be 10% of the uniaxial compressive strength, the residual strength coefficient is set to 0.1 and the internal

friction angle (φ) is taken as 30° (Zhu and Tang 2004; Wang et al. 2009). The uniaxial compressive strength and elastic modulus of the floor and roof in these models are given sufficiently high values to ensure that they do not fail during collapse of the pillars. The properties of the floor and roof are listed in Table 4.

In the Type I model, the mesh size for each pillar is taken as 200 × 150 with 30,000 elements being used to discretize a specimen 4 m wide × 3 m high. For Type II, the mesh size of each pillar is 150 × 300 with 45,000 elements used to simulate a 3 m × 6 m pillar. For the Type III model, the mesh size is 200 × 400 with 80,000 elements being employed to discretize a pillar 4 m wide × 8 m high. It is noted that, for simplicity, Fig. 1 is just the general schematic serial and parallel numerical model setups. It does not reflect the variations in pillar geometry between Types I, II and III. The following numerical results will reflect the modelled pillar relative widths and heights. It is worth

Table 1 Material parameters for tests of two serial pillars

Two serial pillars		Case 1	Case 2
Elastic modulus	Pillar 1	60 Gpa	60 Gpa
	Pillar 2	60 Gpa	60 GPa
Uniaxial compressive strength	Pillar 1	100 Mpa	100 Mpa
	Pillar 2	100 MPa	100 MPa
Poisson's ratio	Pillar 1	0.25	0.25
	Pillar 2	0.25	0.25
Homogeneity index (m)	Pillar 1	3	3
	Pillar 2	3	3

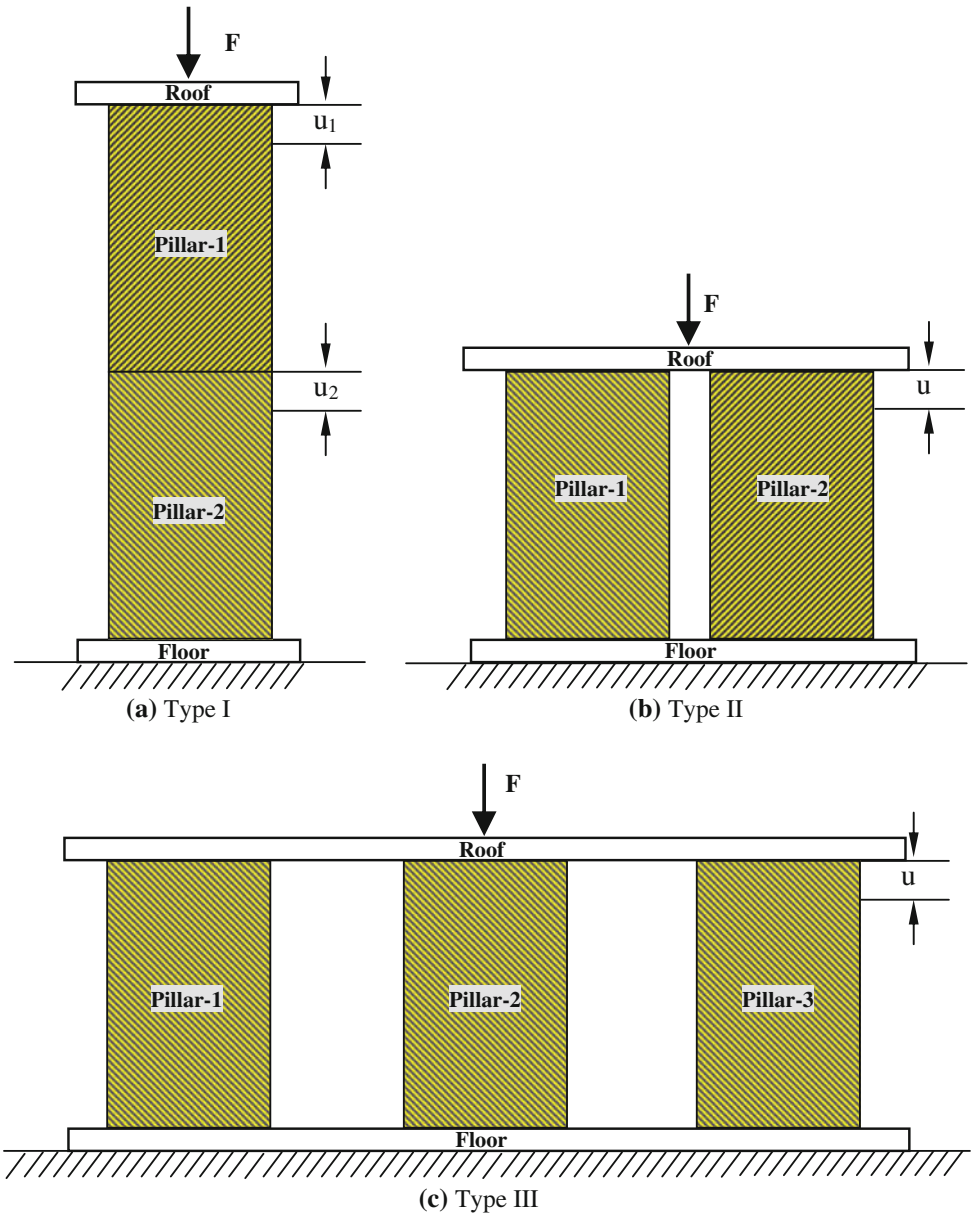

Fig. 1 Schematic serial and parallel numerical model setups without considering the modelled pillar widths and heights. **a** Type I is for the two serial pillars with different uniaxial compressive strengths or elastic moduli; **b** Type II is for parallel pillars with different uniaxial compressive strengths or elastic moduli; **c** Type III is for three parallel pillars with the same uniaxial compressive strengths and elastic moduli, but different homogeneity indices (m)

Table 2 Material parameters for tests of two parallel pillars

Two parallel pillars		Case 1	Case 2
Elastic modulus	Pillar 1	30 GPa	60 GPa
	Pillar 2	30 GPa	30 GPa
Uniaxial compressive strength	Pillar 1	100 MPa	200 MPa
	Pillar 2	200 MPa	200 MPa
Poisson's ratio	Pillar 1	0.25	0.25
	Pillar 2	0.25	0.25
Homogeneity index (m)	Pillar 1	3	3
	Pillar 2	3	3

Table 3 Material parameters for tests of three parallel pillars

Three parallel pillars		Case 1	Case 2
Elastic modulus	Pillar 1	60 GPa	60 GPa
	Pillar 2	60 GPa	60 GPa
	Pillar 3	60 GPa	60 GPa
Uniaxial compressive strength	Pillar 1	200 MPa	200 MPa
	Pillar 2	200 MPa	200 MPa
	Pillar 3	200 MPa	200 MPa
Poisson's ratio	Pillar 1	0.25	0.25
	Pillar 2	0.25	0.25
	Pillar 3	0.25	0.25
Homogeneity index (m)	Pillar 1	4	3
	Pillar 2	5	3
	Pillar 3	3	3

Table 4 Material parameters for floor and roof

Elastic modulus	300 GPa
Uniaxial compressive strength	1,000 MPa
Poisson's ratio	0.25
Homogeneity index (m)	3

remarking that the width-to-height (w/h) ratio plays a key role in the uniaxial compressive strength and failure mode of mine pillars (Tang et al. 2000). In the current study, however, these effects are not considered. To simplify the analysis, the effect of the excavation process between pillars is not considered.

All the simulations in this paper assume two-dimensional plane strain conditions with the loading being applied via prescribed displacements, similar to the displacement control used in servo-controlled laboratory tests. Each increment of displacement is equivalent to the disturbance induced by mining, and the pillars are loaded to failure by vertically displacing the upper boundary in increments of 0.005% of the model height (Tang 1997). As the total vertical displacement in the axial direction increases, the stress states in the pillars reach the failure criterion and cause damage. In the finite element analysis, the stress and deformation distribution throughout each specimen is continually adjusted via iterations to satisfy the equilibrium. Due to stress redistribution, the stress state may cause shear failure and lead to further ruptures. For a given external displacement, the iterations are repeated until there are no new failed elements remaining in the sample. Following that, the external displacements are incremented and the process is repeated. During this process, the system forms macroscopic fractures, releasing the elastic energy stored in the elements as acoustic emissions. Ultimately, the entire load–deformation curve is obtained.

3 Numerical Results and Analysis

3.1 Numerical Results for Two Serial Pillars (Type I)

3.1.1 Numerical Results for Case I

For Case I, Fig. 2 shows the failure mode development at selected stages of loading. Figures 3, 4 and 5 show, respectively, the associated stress–strain relation, the AE counts and energy-versus-strain plots for the two serial pillars under increasing vertical displacement. Since the uniaxial compressive strength of pillar 2 (200 MPa) is higher than that of pillar 1 (100 MPa), the initial damage is mainly concentrated in pillar 1 with little damage occurring in pillar 2 (see Fig. 2). During stage (a), the damaged elements are randomly distributed in pillar 1. Due to the heterogeneity of the rock ($m = 3$), some element damage develops with increasing loading, and a localized shear failure zone forms from the top left corner of pillar 1 to the midpoint of the interface of pillar 1 and pillar 2 (Fig. 2 stages b, c and d). During this stage, some AE counts and energy releases occur (see Fig. 4). As soon as the failure zone reaches the interface of pillar 1 and pillar 2, it develops along the interface (stage e) but does not cross it due to the higher uniaxial compressive strength of the second pillar. In this stage, a large stress drop occurs, which indicates that the serial pillar system is no longer stable (Fig. 3 stage e). The peak uniaxial compressive strength reached is 52 MPa, and more AE counts and energy releases occur (stage e of Figs. 4, 5). Although the whole system is unstable after stage e, the system still retains some residual strength of about 15 MPa (Fig. 3 stages f, g and h). Subsequently, the failure zone continues to propagate and begins to rebound from the interface. Several smaller stress drops in the post-peak range (stages f, g and h) are observed when the shear zone extends to the pillar boundary, with each stress drop being associated with elevated acoustic emission counts and energy release rates (Figs. 4, 5). Ultimately, a V-shaped failure zone is formed (Fig. 2 stages f, g and h).

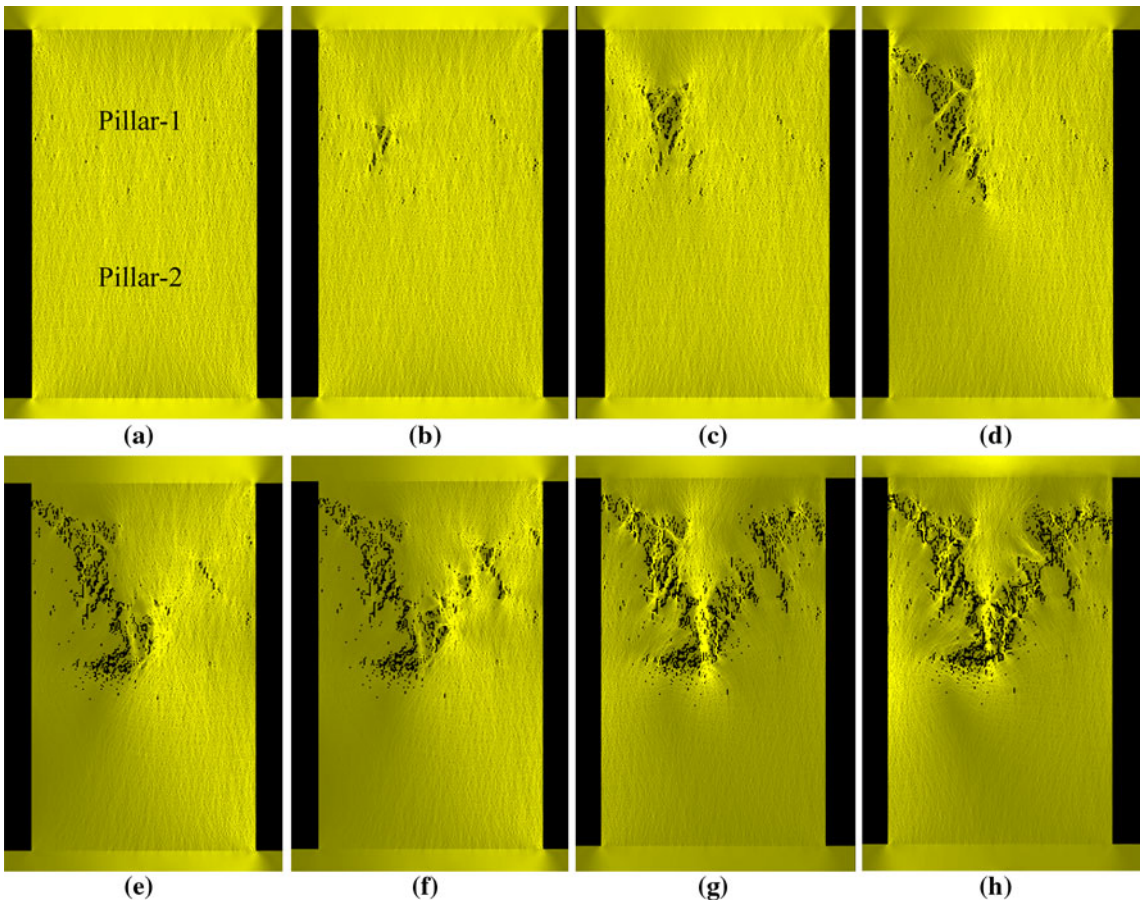

Fig. 2 Failure processes of two serial pillars with different uniaxial compressive strengths, but the same elastic moduli (shear stress distribution)

To explain the above results, consider a simple one-degree-of-freedom system where two elements are connected in series (see Fig. 6). The uniaxial compressive strength of element 2 is higher than element 1, and both elements 1 and 2 are nonlinear and inelastic, possessing softening and hardening characteristics as shown in Fig. 7. From static equilibrium, it follows that:

$$P_1 = P_2 = P, \quad u = u_1 + u_2 \tag{9}$$

where P_1 and P_2 are the forces acting on elements 1 and 2, respectively; u_1 and u_2 are the corresponding displacements.

The force–displacement relation for the overall systems is:

$$P = \frac{f'(u_1)f'(u_2)}{f'(u_1) + f'(u_2)}u \tag{10}$$

Where $f'(u_1)$ and $f'(u_2)$ are the secant moduli of the characteristics $P = P(u_1)$ for element 1 and $P = P(u_2)$ for element 2, respectively.

From Fig. 7, it is seen that there is a limit point, B_1, where the static load control is no longer possible. There is another critical point, C_1, for displacement control where $f'(u_2) = -f'(u_1)$ and $\Delta P/\Delta u = \infty$. This is the condition for instability of the system. The resulting equilibrium stress–strain relation for the whole system is shown in Fig. 3 (stage e).

In addition, when the serial pillar system is loaded from point A_1 to the maximum load of pillar 1 (point B_1), pillar 1 starts to yield as it is weaker than pillar 2. Pillar 2, however, does not fail because of its higher uniaxial compressive strength. This phase corresponds to stages a–d in Fig. 2. During stage 1, the AE events recorded were from the combination of pillars 1 and 2. Afterwards, the load decreases due to the failure of pillar 1, causing pillar 2 to rebound elastically from B_2 to C_2. Point C_1 is the critical point controlling the stability of the system. The stage from points B_1 to C_1 corresponds to stage e in Fig. 2. During this phase, the AE events recorded were those produced by pillar 2, because few AE events were produced by pillar 1 as it was in the process of rebounding (Chen et al. 1997). Points D_1 and D_2 are another stability point, corresponding to stages f, g and h. In summary, the interaction of the two pillars can be explained by the failure of pillar 1 leading to the rebound of pillar 2. The subsequent transfer of energy to pillar 1 from the rebounding pillar 2 accelerates its rate

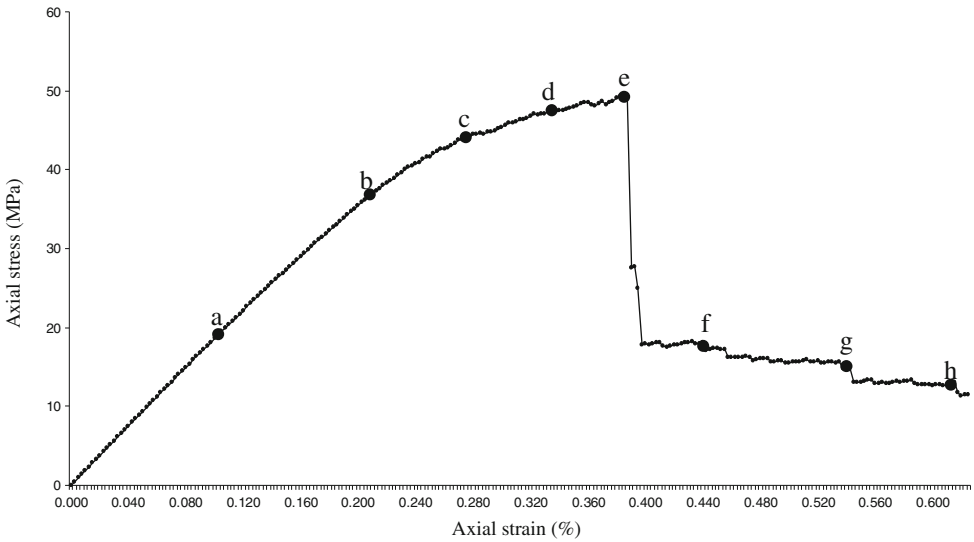

Fig. 3 Axial stress–axial strain relation for two serial pillars with different uniaxial compressive strengths, but the same elastic moduli, Case I

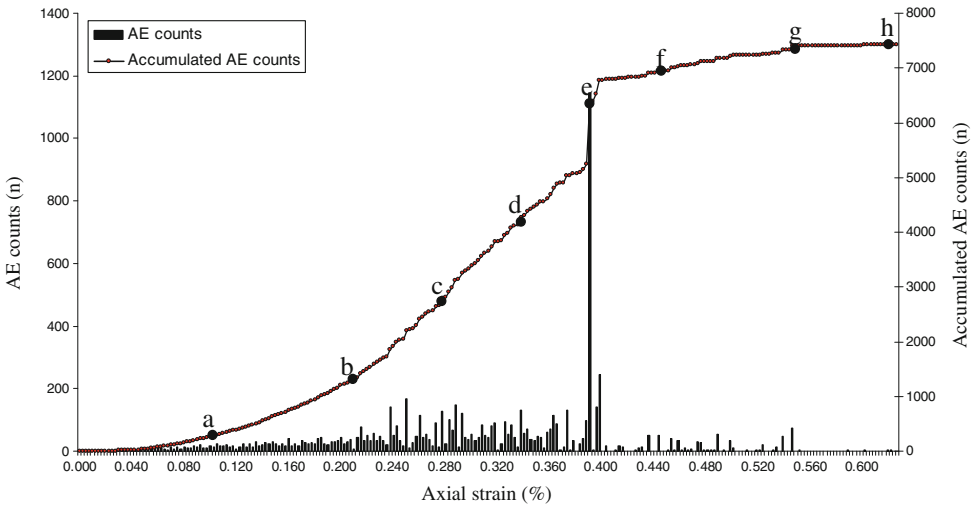

Fig. 4 AE counts versus axial strain for two serial pillars with different uniaxial compressive strengths, but the same elastic moduli, Case I

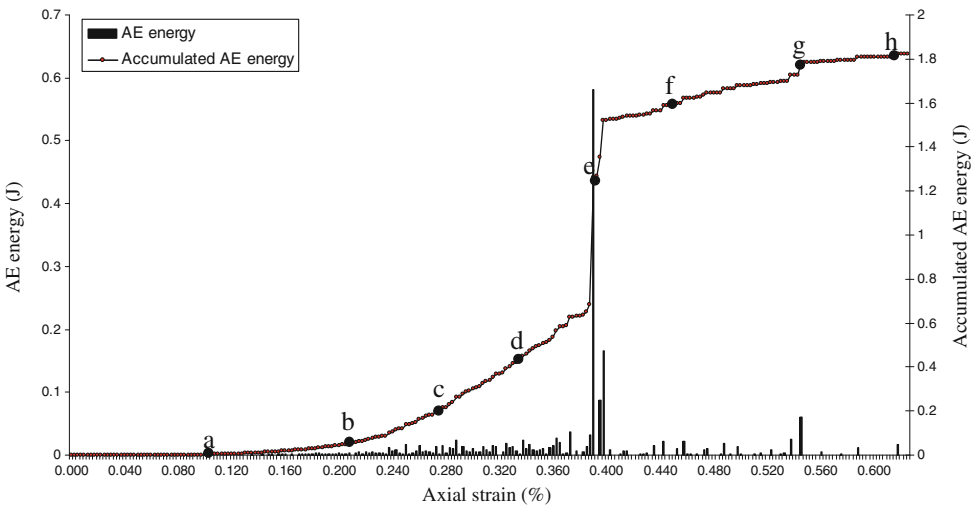

Fig. 5 AE energy versus axial strain for two serial pillars with different uniaxial compressive strengths, but the same elastic moduli, Case I

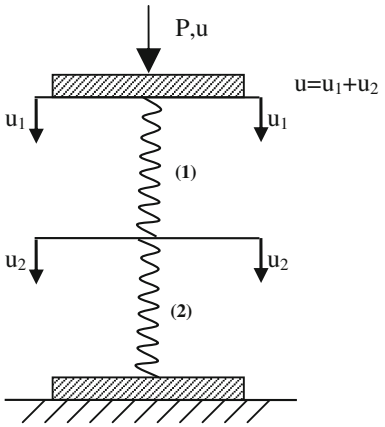

Fig. 6 Schematic system of two elements (pillars) in series

of failure, leading to instability of the whole system (Chen et al. 1997; Kaiser and Tang 1998).

3.1.2 Numerical Results for Case II

For Case II, Fig. 8 shows the failure mode development at selected stages. Figures 9, 10 and 11, respectively, show the axial stress–axial strain relation, the AE counts and energy-versus-axial strain plots for two serial pillars under increasing vertical displacement. Although the uniaxial compressive strengths of pillar 1 and pillar 2 for this case are the same, the elastic modulus of pillar 2 is lower than that of pillar 1, so that it suffers the initial damage [which is mainly concentrated at the interface of the two pillars (Fig. 8, stage a)]. Afterwards, the damaged elements develop and nucleate to form a shear band inside pillar 2 (Fig. 8, stages b and c). Under continuous loading, the shear band starts to traverse the interface and enter pillar 1 (Fig. 8, stage d). In stages e and f of Fig. 8, the shear band bifurcates into two branches in pillar 1, which corresponds to the two stress drops seen in Fig. 9 (stages e and f). Figures 10 and 11 show the corresponding AE counts and energy releases in stages e and f, respectively. In stage g of Fig. 8, the right hand shear branch (stage e) stops propagating upwards, but starts propagating downwards from pillar 1 to pillar 2. The largest stress drop, AE counts and energy releases occur in this stage, whilst stage h represents the residual phase of the serial pillar failure.

As shown in Fig. 12, to explain the above results we note that, whilst the uniaxial compressive strengths of pillar 1 and pillar 2 are the same, due to the lower elastic modulus of pillar 2, it is the first to suffer damage (see Fig. 8, stage a). When pillar 1 rebounds from B_1 to C_1, the failure in pillar 2 is only localized (see Fig. 8, stages b and c). Point C_2 corresponds o corresponding stress drop where $f'(u_2) = -f'(u_1)$. When the prescribed displacement is increased, pillar 1 and pillar 2 are re-loaded and their original yield points are lowered (see Fig. 12). It is possible for pillar 2 to rebound, which leads to failure of pillar 1 at point C'_1, where $f'(u_1)_{\text{new}} = -f'(u_2)_{\text{new}}$. This corresponds to another stress drop with associated AE counts and energy release. This is the reason that the shear band can pass through the interface and enter pillar 1 from pillar 2 (see Fig. 8, stages d, e and f). After several cycles of these processes (i.e. the interaction of the two pillars), the whole system finally becomes unstable.

3.2 Numerical Results for Two Parallel Pillars (Type II)

3.2.1 Numerical Results for Case I

Figure 13 illustrates the failure mode development at selected stages for Case I. Figures 14, 15 and 16 show, respectively, the stress–strain relation, the AE counts and the energy-versus-strain plots for two parallel pillars under increasing vertical displacement. Since the elastic moduli of pillar 1 and pillar 2 are the same, but the uniaxial compressive strength of pillar 2 is greater, the initial

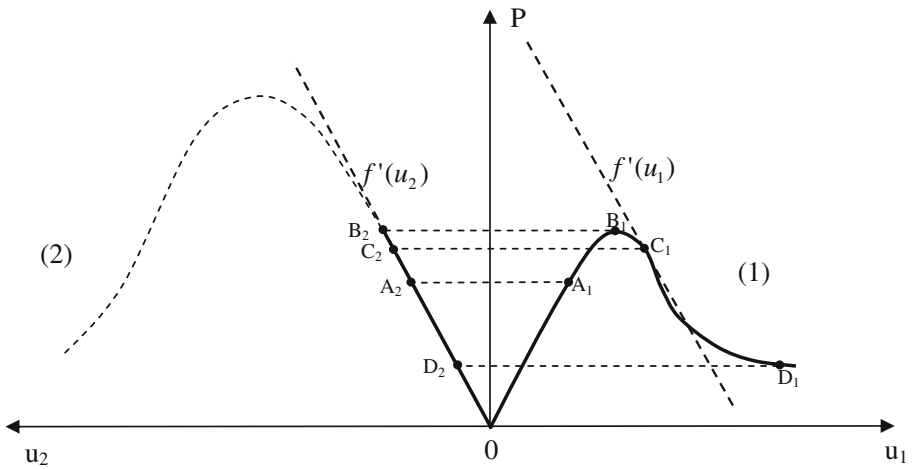

Fig. 7 Schematic serial model with different uniaxial compressive strengths, but the same elastic moduli, Case I (Chen et al. 1997; Kaiser and Tang 1998)

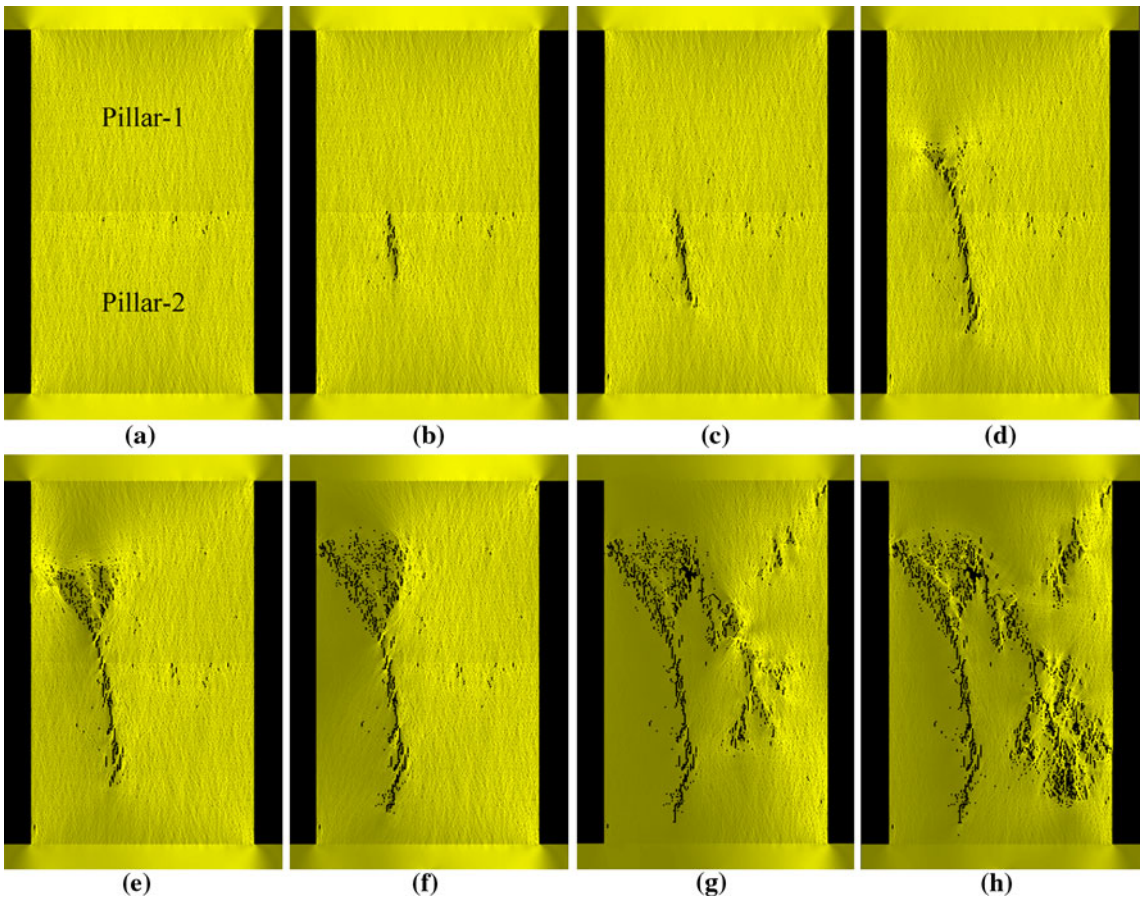

Fig. 8 Failure processes of two serial pillars with the same uniaxial compressive strengths, but different elastic moduli (shear stress distribution), Case II

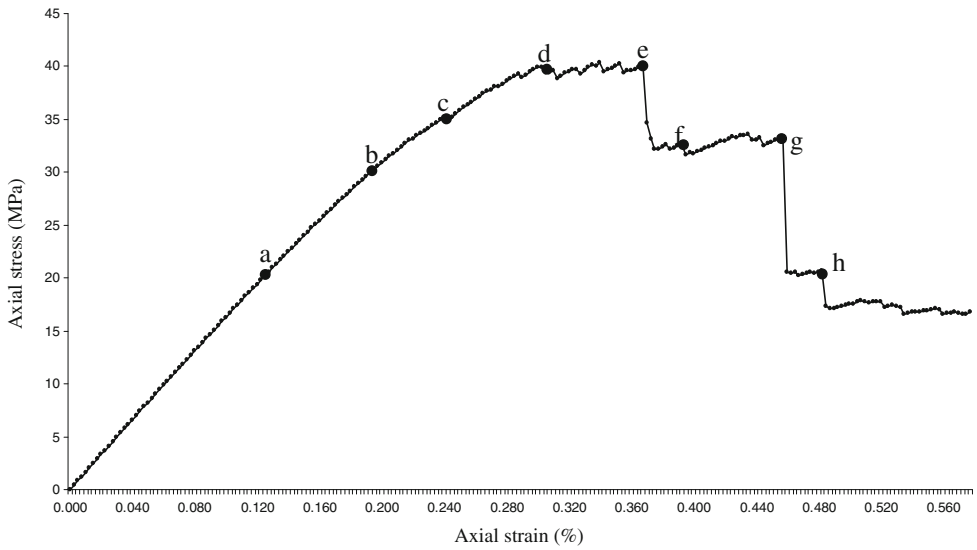

Fig. 9 Axial stress–axial strain relation for two serial pillars with the same uniaxial compressive strengths, but different elastic moduli, Case II

damage occurs in pillar 1 (Fig. 13, stage a). Following this, a shear band forms at an orientation of 55°–60° to the horizontal (Fig. 13, stages b and c). After further loading, another shear band forms from the centre of this shear band in a downward direction (Fig. 13, stage d). In Fig. 14, at point d, there is a big stress drop when pillar 1 becomes unstable. The corresponding AE counts and energy releases are shown at point d of Figs. 15 and 16, respectively.

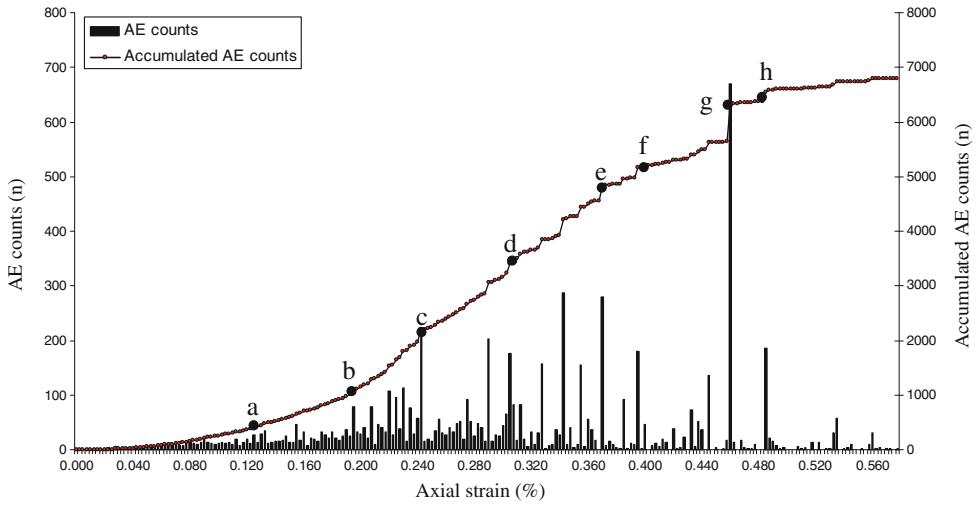

Fig. 10 AE counts versus axial strain for two serial pillars with the same uniaxial compressive strengths, but different elastic moduli, Case II

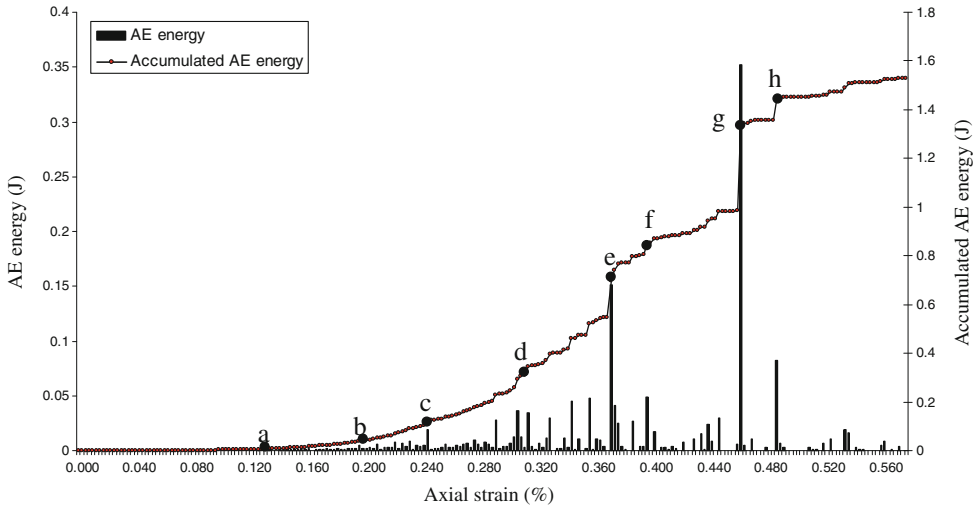

Fig. 11 AE energy versus axial strain for two serial pillars with the same uniaxial compressive strengths, but different elastic moduli, Case II

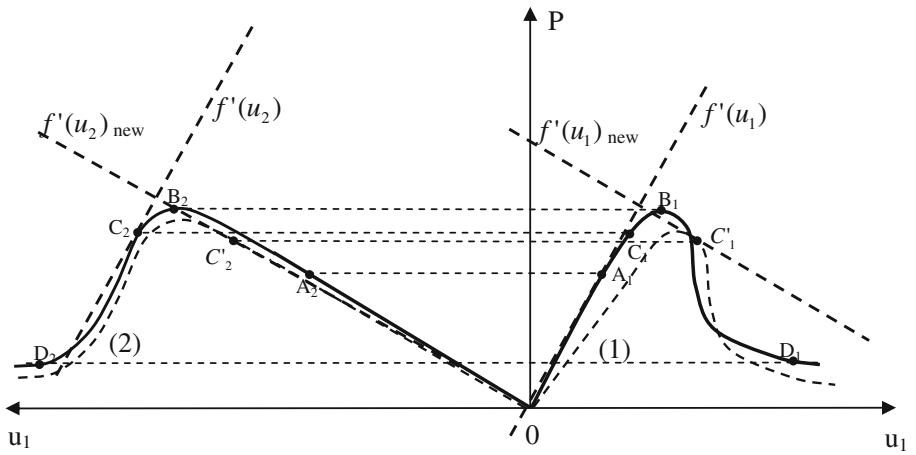

Fig. 12 Schematic serial model with the same uniaxial compressive strengths, but different moduli, Type II

During stages a–d, almost no damaged elements occur in pillar 2. As the condition of pillar 1 deteriorates, pillar 2 bears more of the load and several failure zones start occurring (Fig. 13, stages e and f). Not until stage g do both the pillars become unstable.

It should be noted that another failure zone also develops in pillar 1 from stage e to g. Although pillar 1 becomes unstable at point d in Fig. 14, it still has some uniaxial compressive strength. As the stress-induced damage (microcrack growth) in a rock is irreversible, it is likely

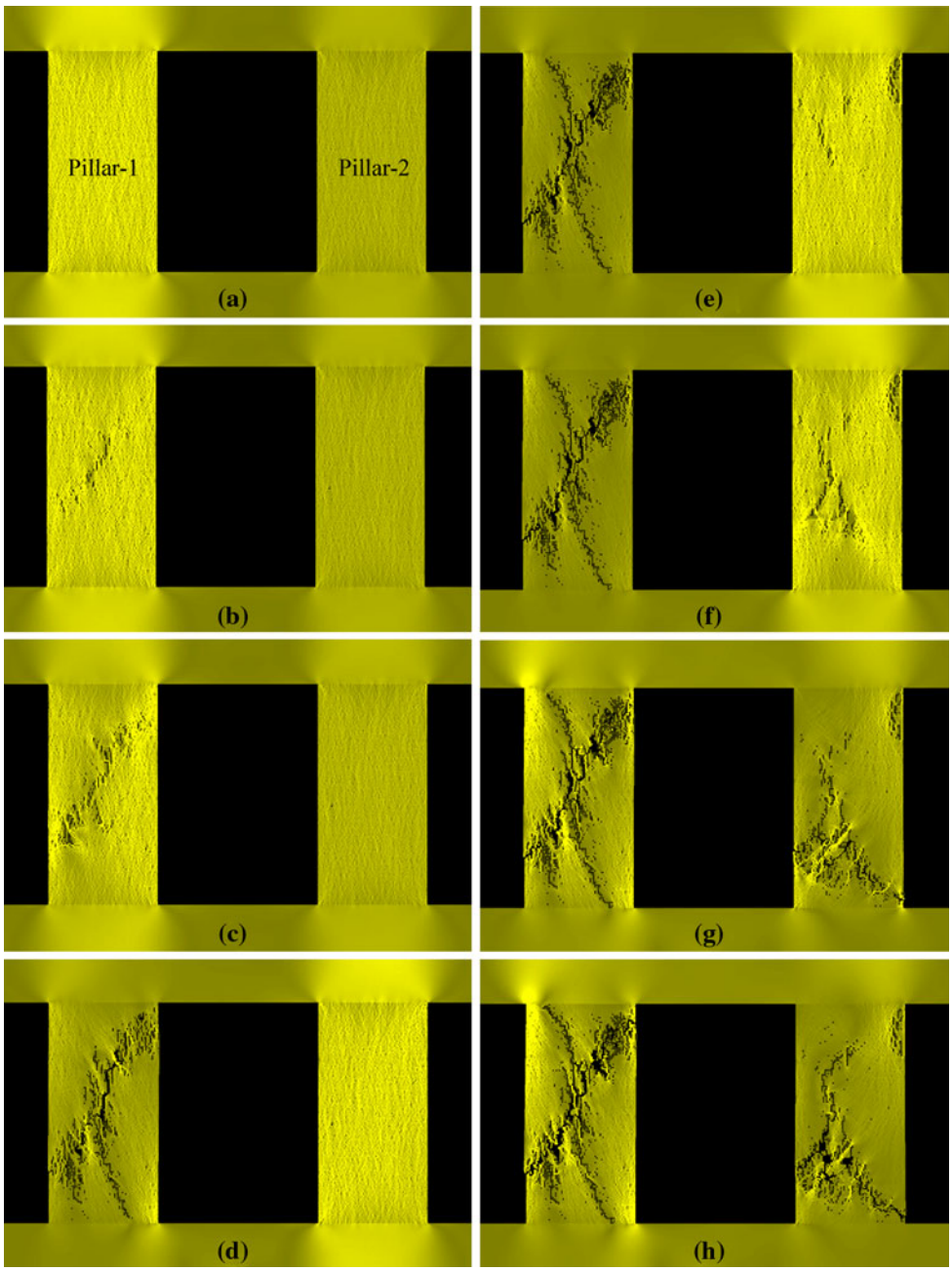

Fig. 13 Failure processes of two parallel pillars with different uniaxial compressive strengths, but the same elastic moduli (shear stress distribution), Case I

that significant new damage will occur only when the previous stress state is exceeded. This is the so-called Kaiser effect in rocks (Kaiser 1950; Tang et al. 1997). In Fig. 14, we see that the second failure zone starts to develop in pillar 1 when the stress level becomes higher (point e) than the previous stress levels (point d). Ultimately, the final failure pattern becomes x-shaped.

To illustrate these phenomena, consider the simple parallel system shown in Fig. 17. Figure 18 presents the associated axial load–deformation response, where the elastic moduli of elements (pillars) 1 and 2 are identical, but the uniaxial compressive strength of element 2 is higher than element 1. Denoting the displacements and forces acting on elements 1 and 2 by u_1, P_1, u_2 and P_2, static equilibrium gives:

$$P = P_1 + P_2, \quad u = u_1 = u_2 \tag{11}$$

whilst the overall force–displacement relation is:

$$P = (f'(u_1) + f'(u_2))u \tag{12}$$

where $f'(u_1)$ and $f'(u_2)$ are the secant moduli of the characteristics $P = P(u_1)$ for element 1 and $P = P(u_2)$ element 2, respectively.

In Fig. 18c, the energy released due to the failure of element 1 equals the area A–B–C, whilst the energy input due to further loading equals the area C–D–E. Only when

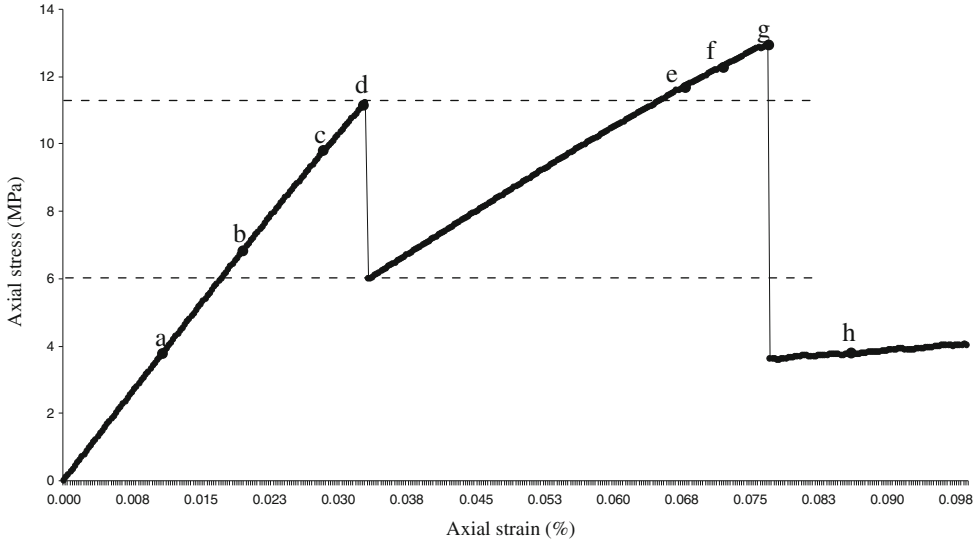

Fig. 14 Axial stress–axial strain relation for two parallel pillars with different uniaxial compressive strengths, but the same elastic moduli, Case I

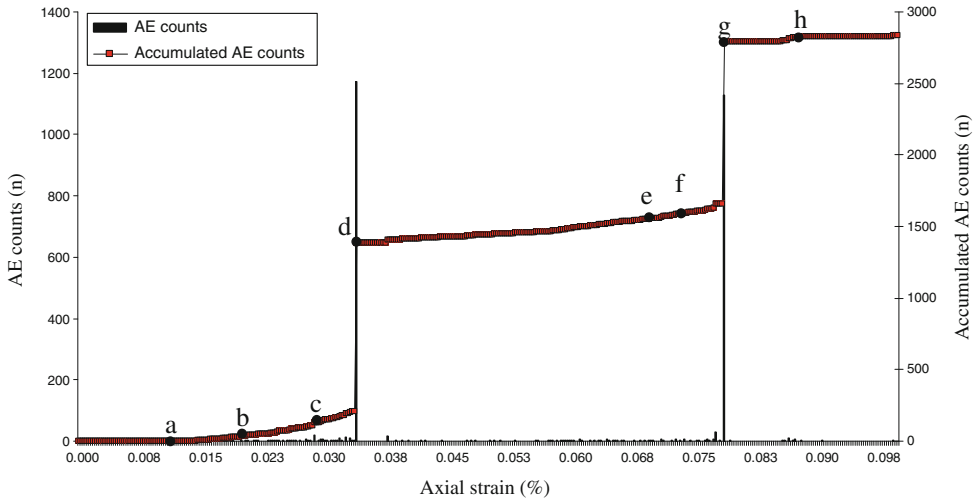

Fig. 15 AE counts versus axial strain for two parallel pillars with different uniaxial compressive strengths, but the same elastic moduli, Case I

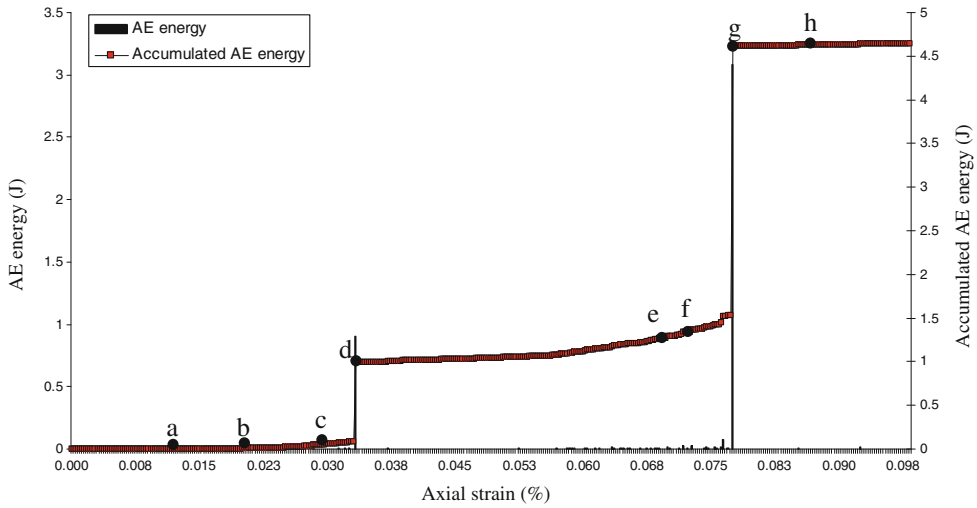

Fig. 16 AE energy versus axial strain for two parallel pillars with different uniaxial compressive strengths, but the same elastic moduli, Case I

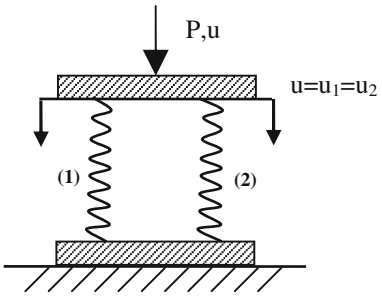

Fig. 17 Schematic system of two elements (pillars) in parallel, Type II

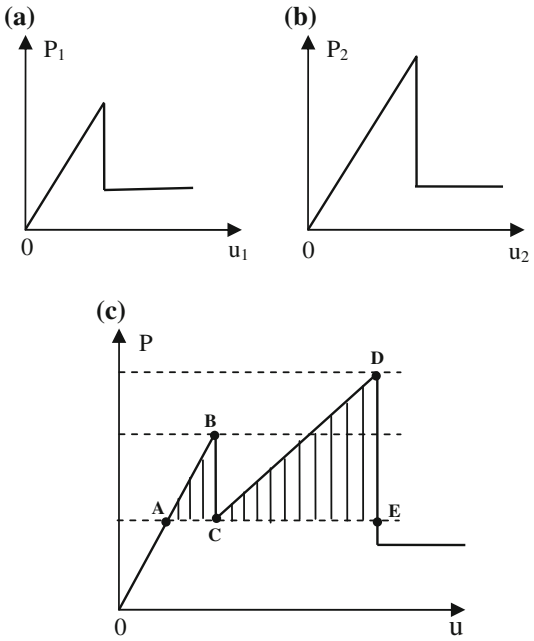

Fig. 18 Schematic system of two elements (pillars) in parallel: **a** and **b** are the load deformation relations for elements (pillars) 1 and 2, which have different uniaxial compressive strengths but the same elastic moduli; Case I. **c** The total load deformation relation for the two pillars in parallel, Case I

the additional energy input exceeds the released energy will further damage occur in element 1. As the area of C–D–E is larger than that of A–B–C, further damage in element (pillar) 1 is inevitable.

3.2.2 Numerical Result for Case II

Figure 19 shows the failure mode development at selected stages of Case II where the uniaxial compressive strength of the pillars is the same, but their moduli are different. Figures 20, 21 and 22 show, respectively, the axial stress–axial strain relation, the AE counts and energy-versus-axial strain plot. From Fig. 19, we see that both pillars bear the same load during the initial phase of (stage a). Under further loading, distinct shear bands form in pillar 2, which has the lowest modulus, whilst little damage occurs in pillar 1 (Fig. 19, stages b and c). At stage d of Fig. 19, pillar 2 becomes unstable and a large loss of load capacity is observed (see also Fig. 20). This generates high AE counts and significant amount of energy release is shown at point d in Figs. 21 and 22, respectively. Subsequently, a failure zone develops in pillar 1. With further loading, a failure zone evolves in pillar 1 (stages e and f) until overall instability sets in (stage g).

Note that during stages e, f and g, no new damage occurs in pillar 2. This is related to the Kaiser effect, and follows from the fact that the previous highest stress state (point d in Fig. 20) is not exceeded by the stress state at point g in Fig. 20. Figure 23 shows a schematic system of two pillars in parallel, with (a) and (b) being the load–deformation relations for elements 1 and 2 and (c) being the overall load–deformation response. In Fig. 23c, the energy released due to the failure of pillar 2 equals the area A–B–C, whilst the energy input due to further loading equals the area C–D–E. Since the area of C–D–E is smaller than that of A–B–C, pillar 1 does not undergo further damage prior to failure.

3.3 Numerical Results for Three Parallel Pillars (Type III)

In this section, two cases of three parallel pillars are considered. To examine the effects of the homogeneity index (m) on the failure mode of the pillars, the elastic moduli and uniaxial compressive strengths for the two cases are the same. For Case I, the homogeneity indices (m) for pillars 1, 2 and 3 were 4, 5 and 3, respectively. As a comparison, for Case II, the homogeneity index for the three pillars was the same ($m = 3$). Table 3 lists the detailed input parameters.

3.3.1 Numerical Results for Case I

For Case I, Fig. 24 shows the failure mode development at selected stages. Figures 25, 26 and 27 show, respectively, the axial stress–axial strain relation, the AE counts and the energy-versus-strain plots for the three parallel pillars under increasing vertical displacement. At stage a in Fig. 25, each pillar bears the same load, and minor damage occurs in each of them. With further loading at stage b, a failure zone forms in the most heterogeneous pillar, which is pillar 3 ($m = 3$). At stage c, the failure zone develops into a diagonal shear band and significant damage occurs in pillar 1 ($m = 4$). Further loading to stage d causes pillar 3 to become unstable, as shown in Figs. 25, 26 and 27 respectively.

Following the failure of pillar 3, the other pillars bear most of the load apart from small residual load capacity.

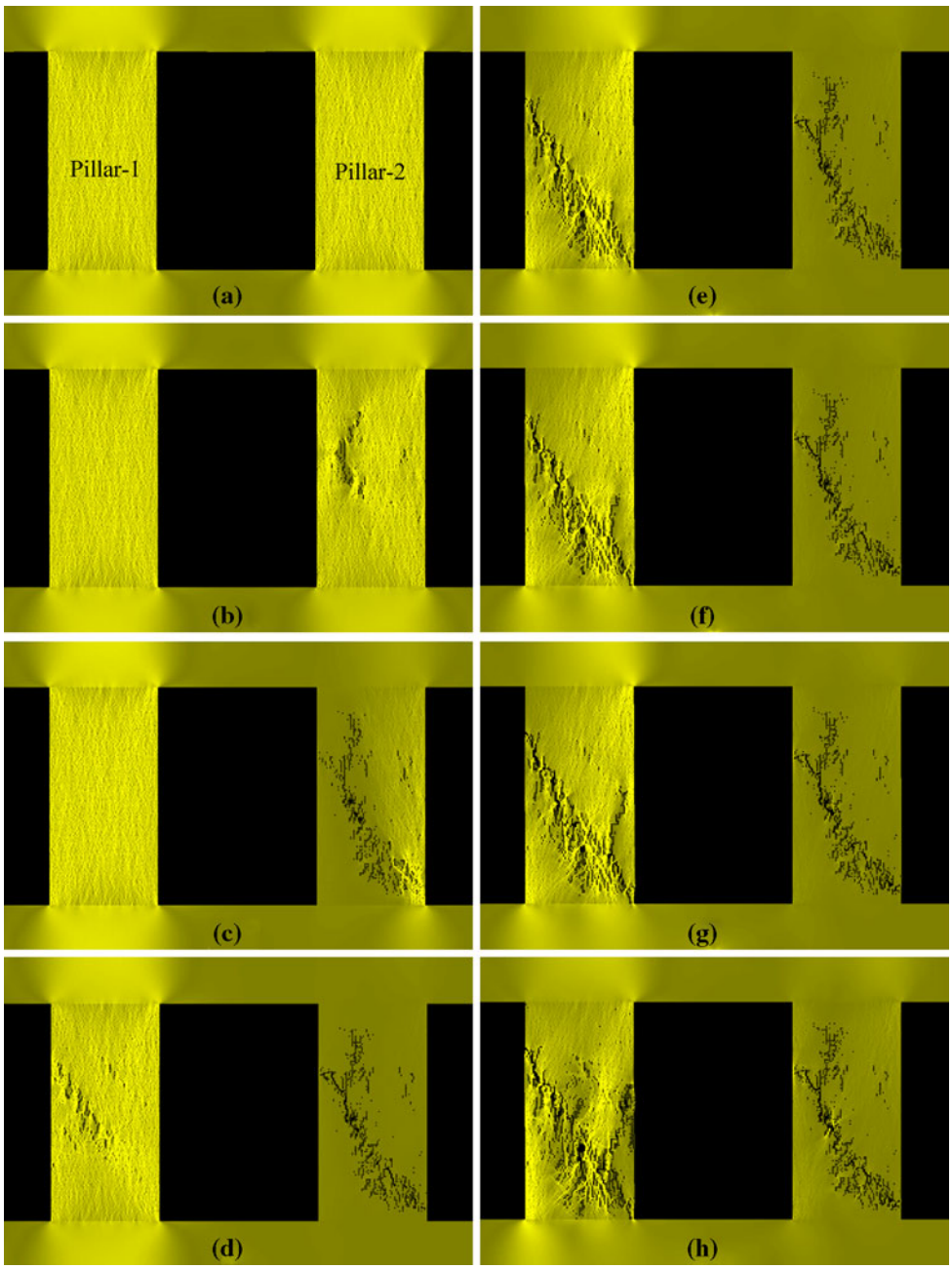

Fig. 19 Failure processes of two parallel pillars with different elastic moduli, but the same uniaxial compressive strengths (shear stress distribution), Case II

Point e in Figs. 25, 26 and 27 shows the stress drop, the AE counts and energy released, respectively, for the overall system. During the loading t from stage a to stage e, almost no new damage occurs in pillar 2. Not until pillar 1 and pillar 3 both fail, does pillar 2 start developing a shear band (stage f) and finally become unstable (stage g). In summary, whilst the uniaxial compressive strength and elastic modulus were the same for the three pillars, the homogeneity index also played an important role in the failure sequence of the pillars. Pillars with a lower homogeneity index failed first, whilst those with a higher index failed last.

3.3.2 Numerical Results for Case II

Figure 28 shows the failure mode development at selected stages for Case II. Figures 29, 30 and 31 show, respectively, the associated axial stress–axial strain relation, the AE counts and the energy-versus-axial strain under increasing vertical displacement. As the uniaxial compressive strengths, elastic moduli and homogeneity indices (m) are the same for the three pillars, they carry the same loading. Accordingly, the initial damaged elements are distributed equally amongst all the pillars in Fig. 28 at stage a (which corresponds to the yield point of the whole

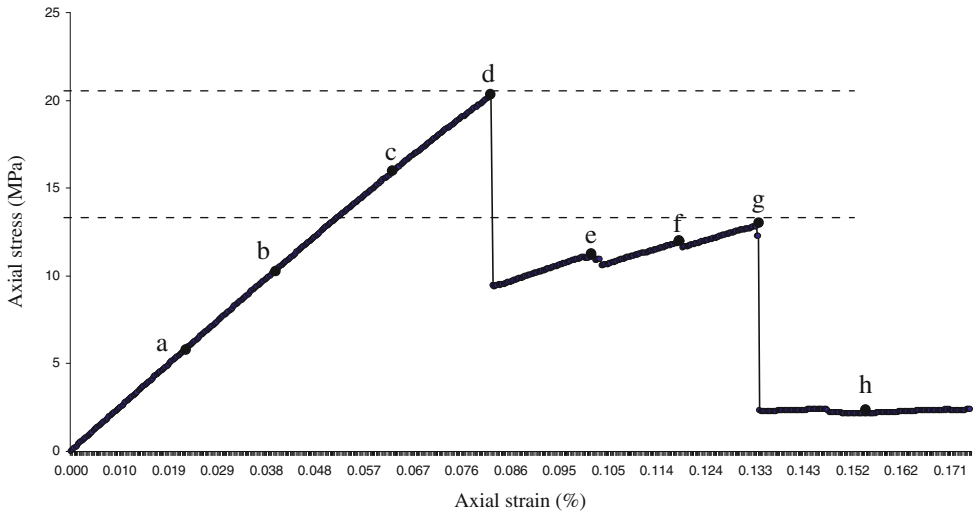

Fig. 20 Axial stress–axial strain relation for two parallel pillars with different elastic moduli, but the same uniaxial compressive strengths, Case II

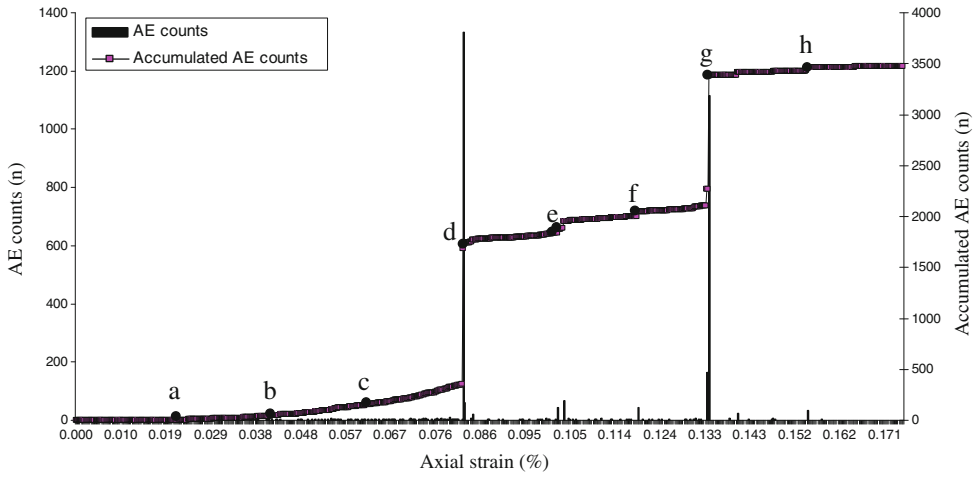

Fig. 21 AE counts versus axial strain for two parallel pillars with different elastic moduli, but the same uniaxial compressive strengths, Case II

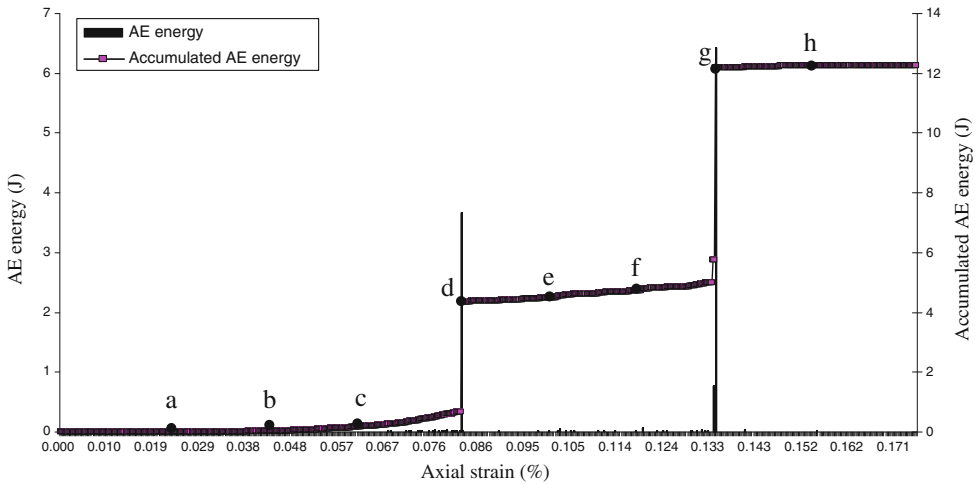

Fig. 22 AE energy versus axial strain for two parallel pillars with different elastic moduli, but the same uniaxial compressive strengths, Case II

system). With further loading, failure zones form in each pillar at different locations (stage b). For example, in pillar 1 and pillar 3, failure zones form on the right-hand side of the pillar, whereas in pillar 2 the failure zone forms at 45° to the horizontal (stage c). Stages d, e, f, g and h depict the subsequent failure process of the three parallel pillars. The points b, c, d, e, f and g in Figs. 29, 30 and 31 show the respective stress drop, AE counts and energy releases

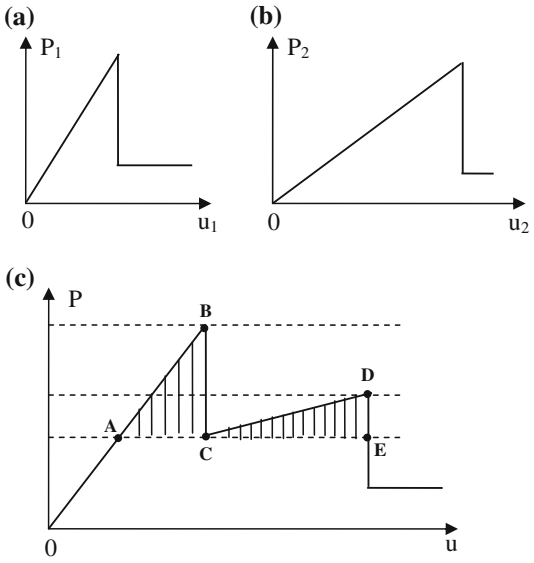

Fig. 23 Schematic system of two elements in parallel: **a** and **b** are the load displacement relations for elements 1 and 2 with different elastic moduli, but the same uniaxial compressive strengths, Case II. **c** The total load displacement relation for two pillars in parallel, Case II

throughout the loading process. All the stress drops are almost the same since the three pillars fail simultaneously, and interaction effects due to elastic rebound are negligible.

4 Conclusions

In this study, the RFPA2D code has been applied to simulate the failure mechanism of serial and parallel rock pillars. Although practical cases are often much more complex than the numerical models considered, the study highlights some interesting phenomena for improving the understanding of pillar-failure mechanisms.

The numerical results show that not only the stiffness, but also the uniaxial compressive strength plays an important role in the stability of rock pillars for the serial and parallel cases considered. For the serial case, the elastic rebound of the rock pillar with a higher uniaxial compressive strength can lead to the sudden failure of the rock pillar with lower uniaxial compressive strength. The corresponding failure

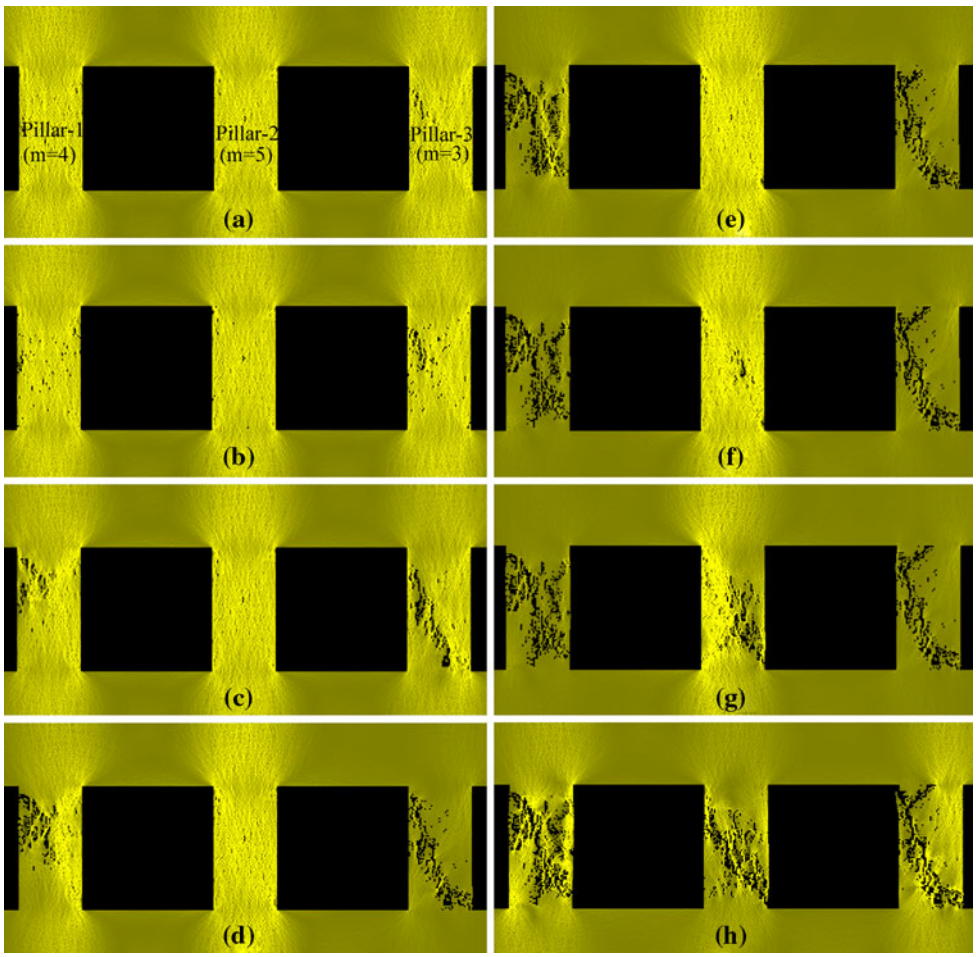

Fig. 24 Failure processes of three parallel pillars with different homogeneity indices, but the same uniaxial compressive strengths and elastic moduli [$m = 4$ (pillar 1), 5 (pillar 2) and 3 (pillar 3), respectively] (shear stress distribution)

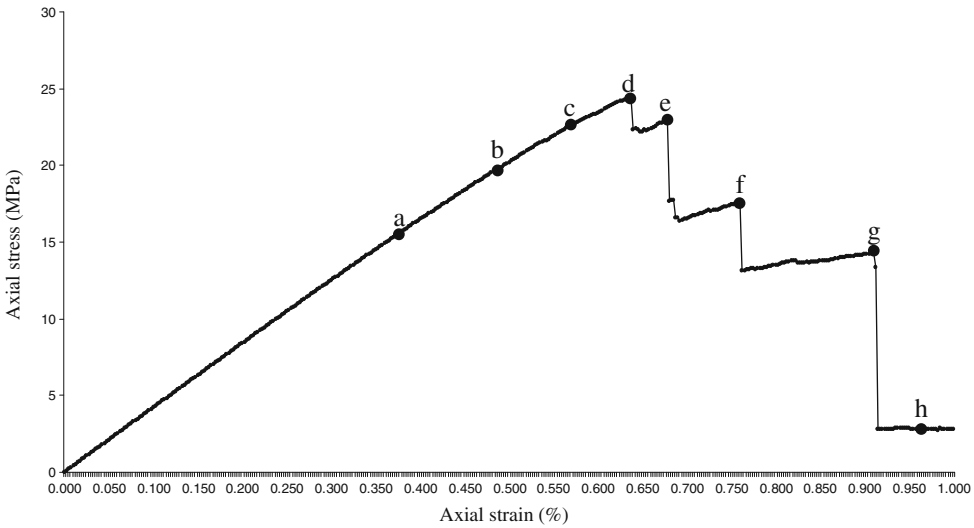

Fig. 25 Axial stress–axial strain relation for three parallel pillars with different homogeneity indices, but the same uniaxial compressive strengths and elastic moduli [$m = 4$ (pillar 1), 5 (pillar 2) and 3 (pillar 3), respectively]

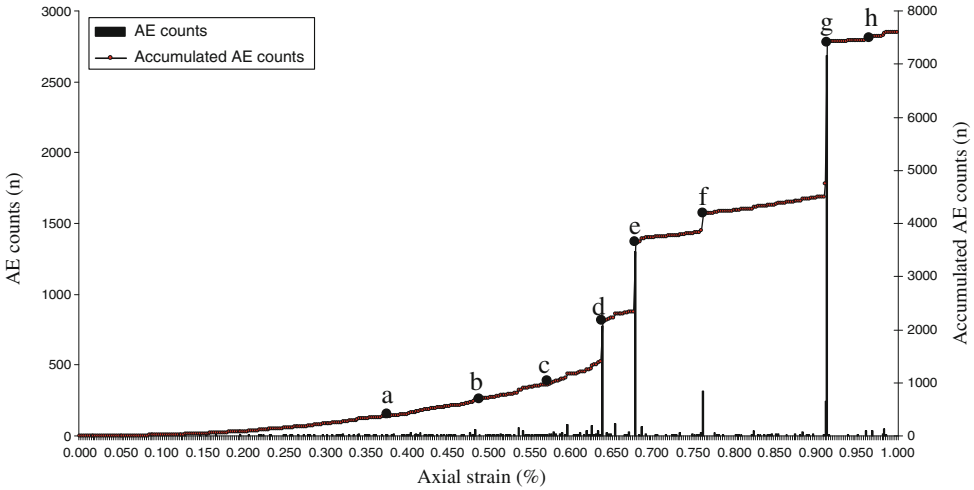

Fig. 26 AE counts versus axial strain for three parallel pillars with different homogeneity indices, but with the same uniaxial compressive strengths and elastic moduli [$m = 4$ (pillar 1), 5 (pillar 2) and 3 (pillar 3), respectively]

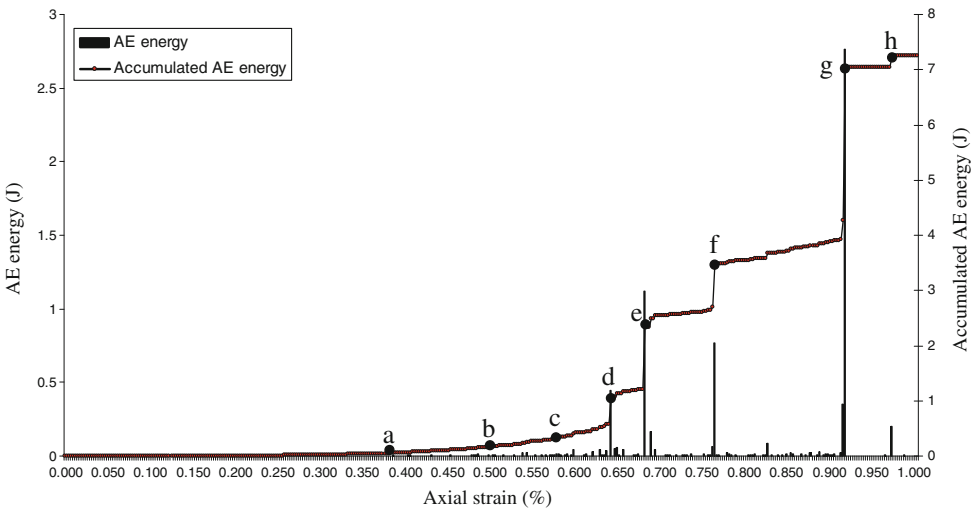

Fig. 27 AE energy versus axial strain for three parallel pillars with different homogeneity indices, but the same uniaxial compressive strengths and elastic moduli [$m = 4$ (pillar 1), 5 (pillar 2) and 3 (pillar 3), respectively]

zone is confined to the pillar with the lower uniaxial compressive strength. In comparison, when the two pillars have the same uniaxial compressive strength but different elastic moduli, both the serial pillars fail. For the parallel case, the damage always occurs in the pillar with the lower uniaxial compressive strength or lower elastic modulus. In addition,

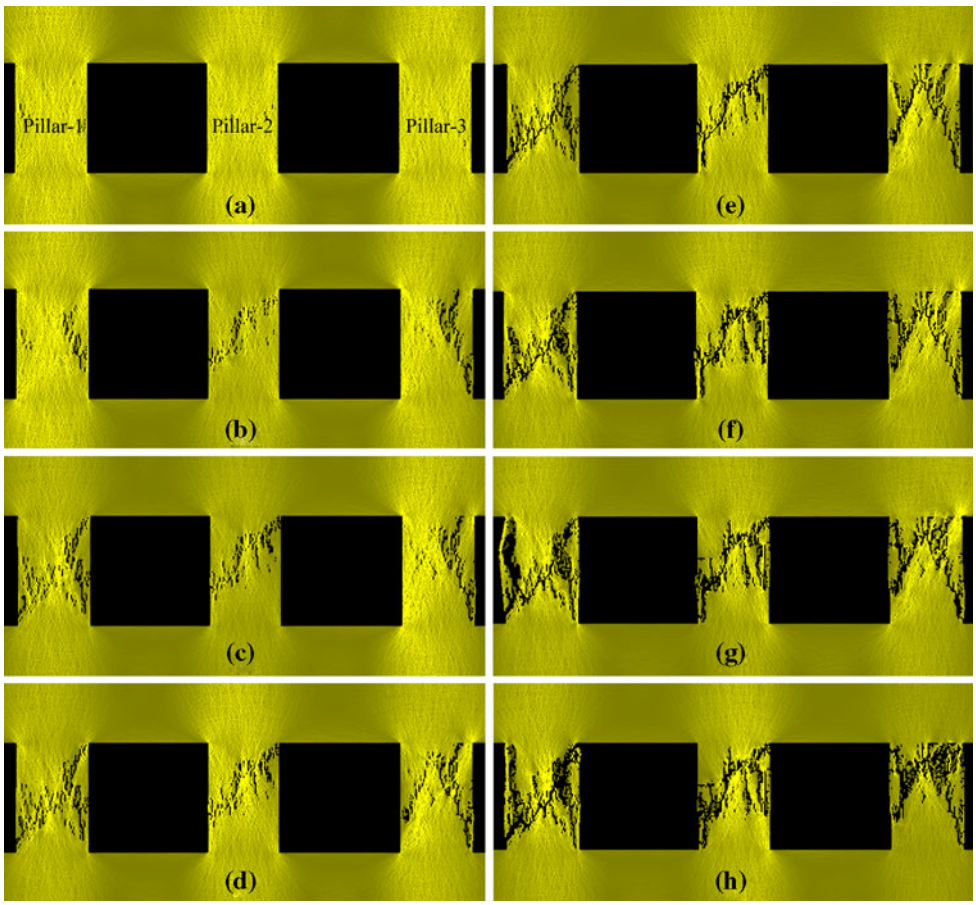

Fig. 28 Failure processes of three parallel pillars with the same homogeneity indices and the same uniaxial compressive strengths and elastic moduli ($m = 3$) (shear stress distribution)

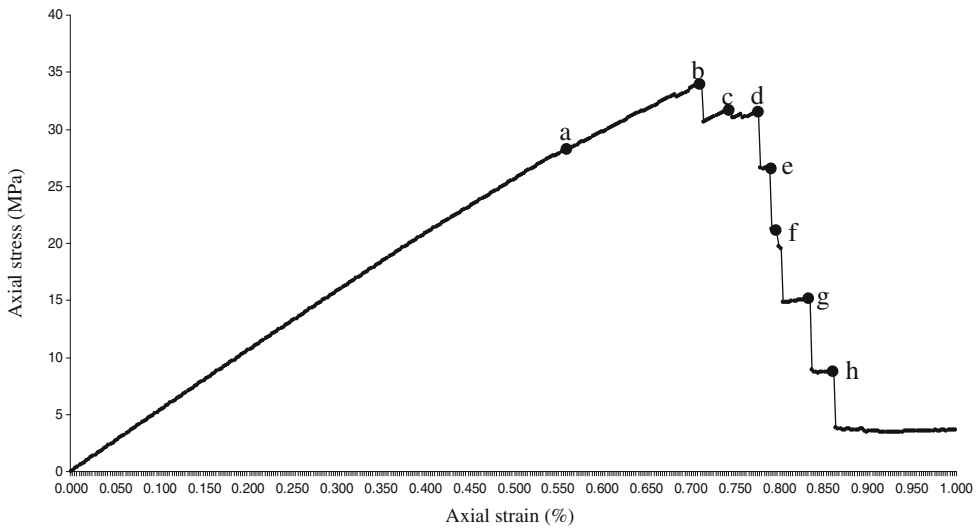

Fig. 29 Axial stress–axial strain relation for three parallel pillars with the same homogeneity indices and the same uniaxial compressive strengths and elastic moduli ($m = 3$)

in accordance with the Kaiser effect, the stress-induced damage in a rock pillar is irreversible. This means that only when the previous stress state in a failed rock pillar is exceeded, or the energy input from the external loading exceeds the previously released energy, does further damage continues to occur.

For cases where the uniaxial compressive strengths and elastic moduli are the same for three parallel pillars, the homogeneity index (m) plays an important role in the failure process. Pillars with the lowest homogeneity index (m) fail first and vice versa. When the uniaxial compressive strength, elastic modulus and homogeneity index are all the

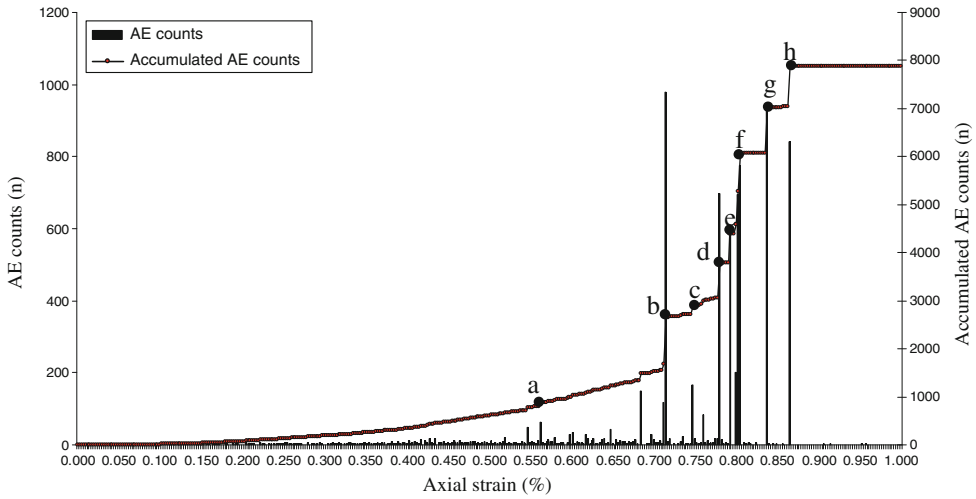

Fig. 30 AE counts versus axial strain for three parallel pillars with the same homogeneity indices and the same uniaxial compressive strengths and elastic moduli ($m = 3$)

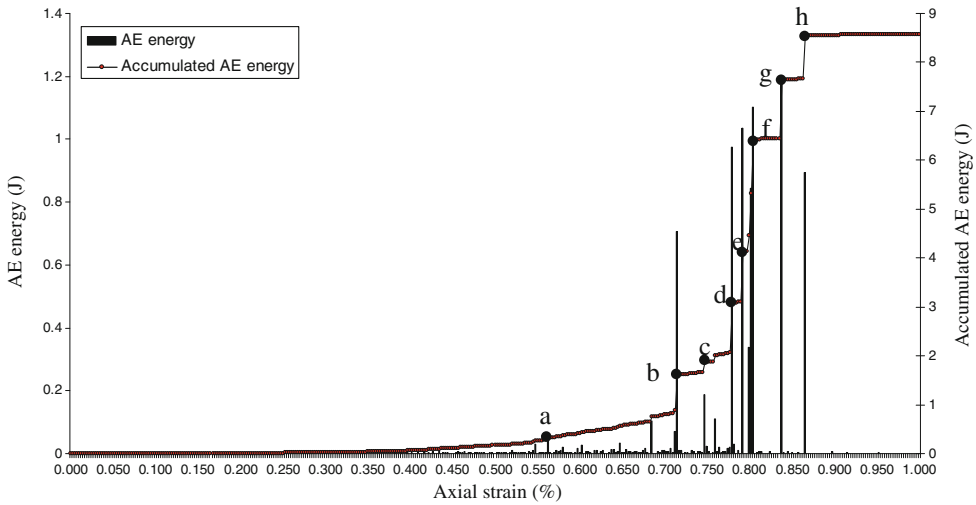

Fig. 31 AE counts versus axial strain for three parallel pillars with the same homogeneity indices and the same uniaxial compressive strengths and elastic moduli ($m = 3$)

same, each pillar starts failing at the same time, but the failure locations are different.

Acknowledgments The work described in this paper was partially supported by the Australian Research Council Grant DP0881238, for which the authors are very grateful.

References

Amitrano D (1999) From diffuse to localized damage through elastic interaction. Geophys Res Lett 2(14):2109–2112

Chen ZH, Tang CA, Huang RQ (1997) A double rock sample model for rockbursts. Int J Rock Mech Min Sci 34(6):991–1000

Chen SL, Lee SC, Gui MW (2009) Effects of rock pillar width on the excavation behavior of parallel tunnels. Tunn Undergr Space Technol 24:148–154

Cook NGW (1976) Seismicity associated with mining. Engng Geol 10:99–122

Fang Z, Harrison JP (2002) Numerical analysis of progressive fracture and associated behaviour of mine pillars by use of a local degradation model. Trans Instn Min Metall 111:59–72

Gill DE, Aubertin M, Simon R (1993) A practical engineering approach to the evaluation of rockburst potential. In: Young RP (ed) Rockbursts and seismicity in mines, pp 63–68

Hudson JA, Crouch SL, Fairhurst C (1972) Soft, stiff and servo-controlled testing machines: a review with references to rock failure. Engng Geol 6:155–189

Kaiser J (1950) An investigation into the occurrence of noises in tensile tests or a study of acoustic phenomena in tensile tests. Ph.D thesis, Tech. Hosch. Munchen, Munich, Germany

Kaiser PK, Tang CA (1998) Numerical simulation of damage accumulation and seismic energy release during brittle rock failure. Part II: Rib pillar collapse. Int J Rock Mech Min Sci 35(2):123–134

Krajcinovic D (1996) Damage mechanics. North-Holland, Elsevier, The Netherlands, Amsterdam

Mortazavi A, Hassani FP, Shabani M (2009) A numerical investigation of rock pillar failure mechanism in underground openings. Comput Geotech 35:691–697

Murali Mohan G, Sheorey PR, Kushwaha A (2001) Numerical estimation of pillar strength in coal mines. Int J Rock Mech Min Sci 38:1185–1192

Salamon M (1970) Stability instability and design of coal pillar workings. Int J Rock Mech Min Sci 7:613–631

Sheorey PR (1993) Design of coal pillar arrays and chain pillars. Comprehensive rock engineering, vol 2. Pergamon, Oxford, pp 631–670

Tang CA (1997) Numerical simulation of progressive rock failure and associated seismicity. Int J Rock Mech Min Sci 34:249–262

Tang CA, Hudson JA, Xu XH (1993) Rock failure instability and related aspects of earthquake mechanisms. China Coal Industry, Beijing

Tang CA, Chen ZH, Xu XH, Li C (1997) A theoretical model of the Kaiser effect in rock. Pure Appl Geophys 150:203–215

Tang CA, Tham LG, Lee PKK, Tsui Y, Liu H (2000) Numerical tests on micro–macro relationship of rock failure under uniaxial compression, Part II: constraint, slenderness and size effects. Int J Rock Mech Min Sci 37(4):570–577

van der Merwe JN (1998) Practical coal mining strata control: a guide for managers and supervisors at all levels. Itasca Africa Ltd, South Africa

Wang SY, Lam KC, Au SK, Tang CA (2006) Analytical and numerical study on the pillar rockburst mechanism. Rock Mech Rock Engng 39:445–467

Wang SH, Lee CI, Ranjith PG, Tang CA (2009) Modeling the effect of heterogeneity and anisotropy on the excavation damaged/disturbed zone (EDZ). Rock Mech Rock Engng 42:229–258

Weibull W (1939) A statistical theory of the strength of materials. Ing Vet Ak Handl 151:5–44

Zhu WC, Tang CA (2004) Micromechanical model for simulating the fracture process of rock. Rock Mech Rock Engng 37(1):25–56